# Numerical validation of the quantum lattice Boltzmann scheme in two and three dimensions

S. Palpacelli[1] and S. Succi[2]
[1]*Dipartimento di Matematica, Università Roma Tre, Largo San Leonardo Murialdo 1, 00146, Roma, Italy*
[2]*Istituto Applicazioni del Calcolo, Viale Policlinico 137, 00161 Roma, Italy*
(Received 18 January 2007; published 15 June 2007)

The multidimensional formulation of the quantum lattice Boltzmann (QLB) scheme is validated against analytical solutions of the time-dependent nonrelativistic Schrödinger equation in two and three spatial dimensions. As a result, we demonstrate the viability of the quantum lattice Boltzmann scheme for the numerical solution of the time-dependent Schrödinger equation in multiple spatial dimensions. In addition, the links between the QLB scheme and sequential splitting methods for partial differential equations are also clarified.

DOI: 10.1103/PhysRevE.75.066704 PACS number(s): 02.70.−c, 03.65.−w

## I. INTRODUCTION

In the last decade the lattice kinetic approach to fluid dynamics, and notably the lattice Boltzmann (LB) method, has consolidated into a powerful alternative to the discretization of the Navier-Stokes equations for the numerical simulation of a wide range of complex fluid flows [1–4]. To date, the overwhelming majority of LB work has been directed to the investigation of classical (nonquantum) fluids. Nonetheless, a small group of authors have also investigated lattice kinetic formulations of quantum mechanics [5–9]. The earliest LB model for quantum motion built upon a formal analogy between the Dirac equation and a Boltzmann equation for a complex distribution function [10–12]. It was then shown that the nonrelativistic Schrödinger equation derives from the complex Boltzmann equation under the same adiabatic assumptions (in imaginary time) which take the Boltzmann equation for classical molecules into the Navier-Stokes equations of continuum fluid mechanics. Based on this analogy, a quantum lattice Boltzmann scheme was formulated, in which the discrete speeds are identified with the four-spinor components of the Dirac's wave function. For $(1+1)$-dimensional problems (evolutionary problems in one spatial dimension) this identification is fairly natural, since the spin can always be aligned with momentum (unit helicity). In higher dimensions, however, such a helicity-1 representation is no longer viable because the spin does not transform like ordinary vectors, and consequently the Dirac propagation matrices cannot be diagonalized simultaneously. To cope with this problem, the classical stream-collide structure of the Boltzmann equation was augmented with a "rotation" step, designed in such a way as to secure alignment between momentum and spin degrees of freedom along each direction of propagation (operator splitting). To the best of our knowledge, to date, such a multidimensional version of the quantum lattice Boltzmann (QLB) scheme has not been validated by actual numerical simulations. In this paper, we present such a validation for the case of a free particle and the harmonic oscillator in both two and three dimensions.

Our numerical results show satisfactory agreement with the analytical solutions, thereby proving the viability of three-step, stream-collide-rotate, theoretical structure of the multidimensional QLB scheme. Finally, a few comments on the potential use of QLB-like schemes for prospective quantum computer implementations are also presented.

## II. REVIEW OF THE ONE-DIMENSIONAL MODEL

The quantum lattice Boltzmann model proposed in [10,12] is based on a formal analogy between the Dirac equation and the discrete kinetic equation named the lattice Boltzmann equation (LBE). In particular, it is possible to show that the nonrelativistic Schrödinger equation ensues from the relativistic Dirac equation in the adiabatic limit where antisymmetric fast modes are enslaved to the symmetric slow ones. In [10] this was demonstrated for the one-dimensional case, and a theoretical strategy for two and three dimensions was proposed, albeit not tested against numerical simulations.

Let us briefly recall the main ideas behind the quantum lattice Boltzmann scheme in one dimension.

Consider the Dirac equation in one dimension. Using the Majorana representation [13], and projecting upon chiral eigenstates, the Dirac equation reads

$$\begin{aligned}
\partial_t u_1 + c\partial_z u_1 &= \omega_c d_2 + igu_1, \\
\partial_t u_2 + c\partial_z u_2 &= \omega_c d_1 + igu_2, \\
\partial_t d_1 - c\partial_z d_1 &= -\omega_c u_2 + igd_1, \\
\partial_t d_2 - c\partial_z d_2 &= -\omega_c u_1 + igd_2,
\end{aligned} \tag{1}$$

where $u_{1,2}$ and $d_{1,2}$ are complex wave functions composing the Dirac quadrispinor

$$\psi = \begin{pmatrix} u_1 \\ u_2 \\ d_1 \\ d_2 \end{pmatrix},$$

and $\omega_c = mc^2/\hbar$ is the Compton frequency ($c$ is the light speed and $\hbar = h/2\pi$ where $h$ is the Planck constant), $g = qV$ is the space-dependent frequency coupling to the external potential $V$, and $q$ is the particle electric charge.

Nonrelativistic motion is reproduced by the model in the adiabatic limit

 

$$\omega \ll |\omega_c + g|,$$

where $\omega$ is the typical frequency or energy of the solution $\psi$, so that one can estimate $|\partial_t \psi| = \omega |\psi|$.

With the additional constraint of "small" potential interaction

$$|g| \ll \omega_c,$$

it is easy to check that the "slow" mode (to be defined shortly) dynamics is governed by the Schrödinger equation for a spinless particle of mass $m$. In particular, for a free particle ($V=0$), we note that under the unitary transformation

$$\phi^{\pm}_{1,2} = \frac{1}{\sqrt{2}} e^{imt}(u_{1,2} \pm i d_{2,1}),$$

observing that $u_{1,2}$ and $d_{1,2}$ are solutions of Eq. (1) and taking the adiabatic limit, the slow modes $\phi^{+}_{1,2}$ obey the Schrödinger equation for a free particle of mass $m$.

### The QLB model in one dimension

Equation (1) is discretized using classical forward differences for the time derivative, while spatial derivatives are replaced by one-sided discrete differences taken along the streaming directions: forward differences for $u_{1,2}$ and backward differences for $d_{1,2}$ (sometimes called "light-cone propagation"). In addition, the right-hand side of Eq. (1) is discretized through an average between the term at time $t$ and position $z$ and the term at time $t+\Delta t$ and position $z \pm \Delta z$ for $u_{1,2}$ and $d_{1,2}$, respectively.

Using atomic units ($c=1$, $\hbar=1$) and assuming $\Delta z = \Delta t = 1$, we obtain the following scheme

$$\hat{u}_1 - u_1 = \frac{m}{2}(d_2 + \hat{d}_2) + \frac{ig}{2}(u_1 + \hat{u}_1),$$

$$\hat{u}_2 - u_2 = \frac{m}{2}(d_1 + \hat{d}_1) + \frac{ig}{2}(u_2 + \hat{u}_2),$$

$$\hat{d}_1 - d_1 = -\frac{m}{2}(u_2 + \hat{u}_2) + \frac{ig}{2}(d_1 + \hat{d}_1),$$

$$\hat{d}_2 - d_2 = -\frac{m}{2}(u_1 + \hat{u}_1) + \frac{ig}{2}(d_2 + \hat{d}_2), \tag{2}$$

where $\hat{u}_{1,2} = u_{1,2}(z+1, t+1)$, $\hat{d}_{1,2} = d_{1,2}(z-1, t+1)$, $u_{1,2} = u_{1,2}(z,t)$, and $d_{1,2} = d_{1,2}(z,t)$.

The linear system of Eq. (2) is solved algebraically for $\hat{u}_{1,2}$ and $\hat{d}_{1,2}$ and yields the explicit scheme

$$\hat{u}_1 = a u_1 + b d_2,$$

$$\hat{u}_2 = a u_2 + b d_1,$$

$$\hat{d}_1 = a d_1 - b u_2,$$

$$\hat{d}_2 = a d_2 - b u_1, \tag{3}$$

where

$$a = (1 - \Omega/4)/(1 + \Omega/4 - ig),$$

$$b = m/(1 + \Omega/4 - ig),$$

with $\Omega = m^2 - g^2$. Here $m$ represents the dimensionless Compton frequency in lattice units ($\Delta z = \Delta t = c = 1$, $q=-1$).

We note that, in analogy with the classical lattice Boltzmann model for fluid dynamics, the scheme of Eq. (2) can be derived from Eq. (1) by integrating along the characteristics of $u$ and $d$, respectively, and approximating the right-hand side by means of the trapezium rule. Moreover, since the QLB operator is linear, while the classical LB operator is not, the resulting scheme of Eq. (2) can be directly solved for $\hat{u}$ and $\hat{d}$ [as we see in Eq. (3)]. This is in contrast with the classical case where, to avoid implicitness of the scheme, a new distribution function is introduced, which is nonlinearly related to the original one [14]. Such nonlinearity stems from the quadratic dependence of the classical local equilibrium on the fluid speed, as required to describe nonlinear hydrodynamic interactions.

The scheme of Eq. (3) is a lattice Boltzmann equation in matrix form [15], where the collision step is performed by applying the unitary collision matrix

$$Q = \begin{pmatrix} a & 0 & 0 & b \\ 0 & a & b & 0 \\ 0 & -b & a & 0 \\ -b & 0 & 0 & a \end{pmatrix} \tag{4}$$

to the quadrispinor $\psi = (u_1, u_2, d_1, d_2)^T$, and the streaming step consists in propagating $u_{1,2}$ forward and $d_{1,2}$ backward according to the light-cone rule, $\Delta z = c \Delta t$. Note that stability is secured by the unitarity of the collision matrix $Q$ for any value of $\Delta t$. This contrasts with standard explicit schemes, whose numerical stability is constrained by Courant-Friedrichs-Lewy-like inequalities of the form $\Delta t < (2m/\hbar)\Delta z^2$.

## III. EXTENSION TO TWO AND THREE DIMENSIONS: A SURVEY

In this section, we work out the details of the multidimensional quantum LB scheme. For the sake of simplicity, we restrict our discussion to the free-particle case ($V=0$); however, the inclusion of a potential is straightforward.

According to the idea presented in [10], we start from the representation of the Dirac equation in which all the spin matrices are real. For a free particle of mass $m$ in three dimensions (in atomic units $c=1$ and $\hbar=1$), this reads [16]

$$[\partial_t + \alpha^x \partial_x + \beta \partial_y - \alpha^z \partial_z]\psi = -im\alpha^y \psi, \tag{5}$$

where $\alpha$ and $\beta$ are the standard $4 \times 4$ Dirac matrices and $\psi$ is the Dirac quadrispinor. In [10], a formal parallel between the discrete speeds of the LBE and the discrete spin states of the Dirac quadrispinor is proposed in order to solve Eq. (5) by means of a kinetic equation.

The main problem with this idea is that in order to achieve a full correspondence between the LBE and the

Dirac equation, the matrices $\boldsymbol{L}=(\alpha^x,\beta,-\alpha^z)$ should be simultaneously diagonalized, which is clearly forbidden. Here, following the notation introduced in [10], $\boldsymbol{L}$ indicates a set of three two-dimensional arrays of size $4\times4$. However, even though simultaneous diagonalization of the three matrices is impossible [17], we can diagonalize each of them separately in a sequence. This means we need to find two $4\times4$ transformation matrices $Y$ and $X$ such that $\tilde{L}^y=Y^{-1}L^yY$ and $\tilde{L}^x=X^{-1}L^xX$ are diagonal. We have then three equivalent formulations of the same equation, each featuring a diagonal streaming operator along $x$, $y$, and $z$, respectively. Hence, we split the operator and use the one-dimensional LBE three times in sequence.

In practice, this means that collision and streaming are first performed along one direction, then the system is "rotated" using a transformation matrix and collision and streaming are performed again along a second direction. Finally the same procedure is applied to the third direction.

To summarize, the three-step algorithm reads as follows:

(1) (a) Collision along $z$:

$$\psi'(P,t+\Delta t)=\tilde{Q}\psi(P,t),$$

where $P=(x,y,z)$ and $\tilde{Q}$ is the collision matrix [see Eq. (10) for details of the definition of $\tilde{Q}$ in the two-dimensional case].

(b) Streaming along $z$:

$$\psi(P+\Delta z,t+\Delta t)=S_z\psi'(P,t+\Delta t),$$

where $S_z$ is the streaming operator along $z$.

(2) (a) Rotation of the system:

$$\psi_y=Y\psi,\quad \tilde{Q}^y=Y^{-1}\tilde{Q}Y.$$

(b) Collision along $y$:

$$\psi'_y(P+\Delta z,t+\Delta t)=\tilde{Q}^y\psi_y(P+\Delta z,t+\Delta t).$$

(c) Streaming along $y$:

$$\psi_y(P+\Delta y+\Delta z,t+\Delta t)=S_y\psi'_y(P+\Delta z,t+\Delta t),$$

where $S_y$ is the streaming operator along $y$.

(3) (a) Rotation of the system:

$$\psi_{xy}=X\psi_y,\quad \tilde{Q}^{xy}=X^{-1}\tilde{Q}^yX.$$

(b) Collision along $x$:

$$\psi'_{xy}(P+\Delta y+\Delta z,t+\Delta t)=\tilde{Q}^{xy}\psi_{xy}(P+\Delta y+\Delta z,t+\Delta t).$$

(c) Streaming along $x$:

$$\psi_{xy}(P+\Delta x+\Delta y+\Delta z,t+\Delta t)=S_x\psi'_{xy}(P+\Delta y+\Delta z,t+\Delta t),$$

where $S_x$ is the streaming operator along $x$.

Finally the updated value is transformed back

$$\psi(P+\Delta x+\Delta y+\Delta z,t+\Delta t)=Y^{-1}X^{-1}\psi_{xy}(P+\Delta x+\Delta y+\Delta z,t+\Delta t).$$

In [10], the matrix $\tilde{Q}$ is $Q$ itself [see Eq. (4)]. This is not correct (as we will clarify in the following) and leads to a scheme that does not solve the Schrödinger equation in the adiabatic limit. In the next section, we describe the details of the two-dimensional model and show that the evolution of the slow modes $\phi^+_{1,2}$ is governed by the Schrödinger equation.

### Two-dimensional model: Details

Let us consider the two-dimensional version of Eq. (5),

$$[\partial_t+\beta\partial_y-\alpha^z\partial_z]\psi=-im\alpha^y\psi.$$

It is known that the choice of the Dirac matrices is not unique; in fact all possible choices are related by similarity transformations. Therefore, we apply a transformation to the matrices in order to diagonalize $\alpha^z$. In particular, we use the transformation matrix

$$Z=\frac{1}{\sqrt{2}}\begin{pmatrix}0&-1&0&1\\1&0&-1&0\\0&1&0&1\\1&0&1&0\end{pmatrix}. \tag{6}$$

This transformation yields the following equivalent problem:

$$[\partial_t+A_z\partial_z+A_y\partial_y]\psi=C\psi,$$

$$\psi(z,y,0)=\psi_0(z,y), \tag{7}$$

where

$$A_z=\begin{pmatrix}1&0&0&0\\0&1&0&0\\0&0&-1&0\\0&0&0&-1\end{pmatrix},$$

$$A_y=\begin{pmatrix}0&0&-1&0\\0&0&0&-1\\-1&0&0&0\\0&-1&0&0\end{pmatrix},$$

$$C=\begin{pmatrix}0&0&0&m\\0&0&m&0\\0&-m&0&0\\-m&0&0&0\end{pmatrix}.$$

The problem of Eq. (7) is solved by using the operator splitting approach. In particular, we use *sequential splitting* in order to treat separately the two spatial dimensions.

Then, defining the splitting step $\Delta t>0$, for $(n-1)\Delta t<t\leq n\Delta t$, we consider the sequence of initial value problems of the form

$$\partial_t\psi_1^n+A_z\partial_z\psi_1^n=\frac{1}{2}C\psi_1^n,$$

$$\psi_1^n[(n-1)\Delta t]=\psi_2^{n-1}[(n-1)\Delta t], \tag{8}$$

and

$$\partial_t \psi_2^n + A_y \partial_y \psi_2^n = \frac{1}{2} C \psi_2^n,$$

$$\psi_2^n[(n-1)\Delta t] = \psi_1^n(n\Delta t), \tag{9}$$

for $n=1,2,\ldots,N$. To start the procedure we set $\psi_2^0(0)=\psi_0$.

If we suppose we are able to exactly solve these two problems, then the function $\psi_{sp}(z,y,n\Delta t)=\psi_2^n(z,y,n\Delta t)$, defined at points $t_n=n\Delta t$, is called the *splitting solution* of the problem and represents a first-order approximation of the real solution.

The two-dimensional problem is now subdivided into two one-dimensional problems which can be numerically solved by using the lattice Boltzmann model proposed for the one-dimensional case. However, in the two-dimensional version of the model, the collision matrix $\tilde{Q}$ is slightly different from $Q$ of Eq. (4) due to the factor $1/2$ in front of matrix $C$ in Eqs. (8) and (9). In particular, for the free-particle case ($V=0$), $\tilde{Q}$ is given by

$$\tilde{Q} = \begin{pmatrix} \tilde{a} & 0 & 0 & \tilde{b} \\ 0 & \tilde{a} & \tilde{b} & 0 \\ 0 & -\tilde{b} & \tilde{a} & 0 \\ -\tilde{b} & 0 & 0 & \tilde{a} \end{pmatrix}, \tag{10}$$

where $\tilde{a}=(1-\tilde{m}^2/4)/(1+\tilde{m}^2/4)$ and $\tilde{b}=\tilde{m}/(1+\tilde{m}^2/4)$ with $\tilde{m}=m/2$.

Note that, in order to apply the lattice Boltzmann model to the problem of Eq. (9), the equation must be transformed to diagonalize $A_y$. Thus, we need to find the transformation $Y$ such that $Y^{-1}A_yY$ is diagonal, and the same transformation has to be applied to $C$, as well, in order to obtain an equivalent equation. One possible choice for $Y$ is

$$Y = \frac{1}{\sqrt{2}} \begin{pmatrix} -1 & 0 & 0 & 1 \\ 0 & -1 & 1 & 0 \\ 1 & 0 & 0 & 1 \\ 0 & 1 & 1 & 0 \end{pmatrix}.$$

By defining the wave functions

$$\phi_{1,2}^{\pm} = \frac{1}{\sqrt{2}} e^{imt}(u_{1,2} \pm i d_{2,1}),$$

it is possible to verify that if $\psi$ is solution of Eq. (7), then $\phi_{1,2}^{\pm}$ satisfy the following equations:

$$\partial_t \phi_{1,2}^{+} + \partial_z \phi_{1,2}^{-} - i\partial_y \phi_{2,1}^{-} = 0, \tag{11}$$

$$\partial_t \phi_{1,2}^{-} + \partial_z \phi_{1,2}^{+} + i\partial_y \phi_{2,1}^{+} = 2im\phi_{1,2}^{-}. \tag{12}$$

From Eq. (12), after adiabatic elimination of the fast antisymmetric modes

$$|\partial_t \phi_{1,2}^{-}| \ll 2m|\phi_{1,2}^{-}|,$$

we obtain

$$\phi_{1,2}^{-} \approx \frac{1}{2im}(\partial_z \phi_{1,2}^{+} + i\partial_y \phi_{2,1}^{+}),$$

and substituting in Eq. (11), we have

$$i\partial_t \phi_{1,2}^{+} + \frac{1}{2m}\left(\partial_{zz}\phi_{1,2}^{+} + \partial_{yy}\phi_{1,2}^{+}\right) = 0.$$

This shows that the slow symmetric modes $\phi_{1,2}^{+}$ obey the Schrödinger equation for a free particle of mass $m$.

As mentioned above, the procedure proposed in [10] needs a small, and yet significant, correction by a factor 2. In fact, in [10], the operator splitting is performed by taking $\tilde{Q}=Q$. This corresponds to solving the following sequence of problems:

$$\partial_t \psi_1^n + A_z \partial_z \psi_1^n = C\psi_1^n$$

$$\psi_1^n[(n-1)\Delta t] = \psi_2^{n-1}[(n-1)\Delta t],$$

and

$$\partial_t \psi_2^n + A_y \partial_y \psi_2^n = C\psi_2^n,$$

$$\psi_2^n[(n-1)\Delta t] = \psi_1^n[(n)\Delta t],$$

for $(n-1)\Delta t < t \leq n\Delta t$, instead of problems of Eqs. (8) and (9). Hence, we are not solving Eq. (7), but rather the following equations:

$$[\partial_t + A_z\partial_z + A_y\partial_y]\psi = \mathbf{2}C\psi$$

$$\psi(z,y,0) = \psi_0(z,y).$$

Performing the same analysis as above, one sees that the wave functions $\phi_{1,2}^{\pm}$ have to be defined as

$$\phi_{1,2}^{\pm} = \frac{1}{\sqrt{2}} e^{i\mathbf{2}mt}(u_{1,2} \pm i d_{2,1}),$$

so that $\phi_{1,2}^{+}$ now solve

$$i\mathbf{2}\partial_t \phi_{1,2}^{+} + \frac{1}{2m}(\partial_{zz}\phi_{1,2}^{+} + \partial_{yy}\phi_{1,2}^{+}) = 0.$$

This brings up a factor of 2 only on the time derivative term, thereby delivering an incorrect factor of 2 in the governing equation.

## IV. NUMERICAL TEST 1: FREE PROPAGATION

To validate the model in this regime we set, as initial condition, a minimum uncertainty wave packet

$$\psi_0(z,y) = (2\pi\Delta_{0z}\Delta_{0y})^{-1/2} \exp\left(-\frac{(z-z_0)^2}{4\Delta_{0z}^2}\right) \times \exp\left(-\frac{(y-y_0)^2}{4\Delta_{0y}^2}\right) \exp[-im(v_z z + v_y y)]. \tag{13}$$

This is a wave packet centered about $(z_0,y_0)$ with initial

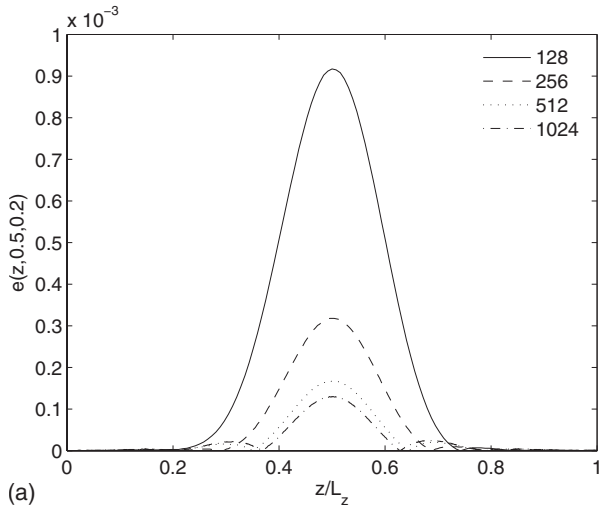


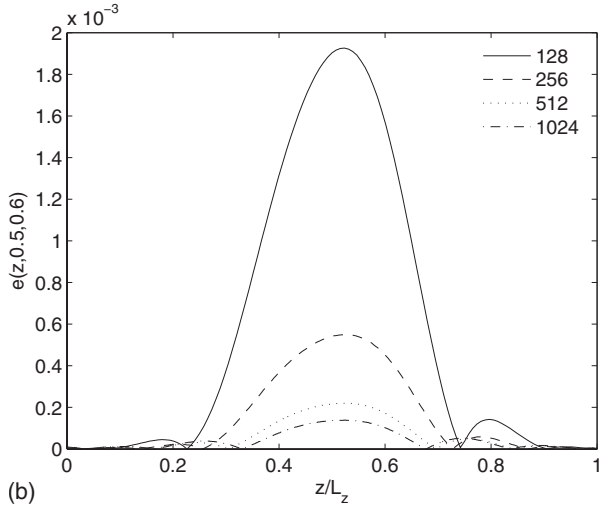


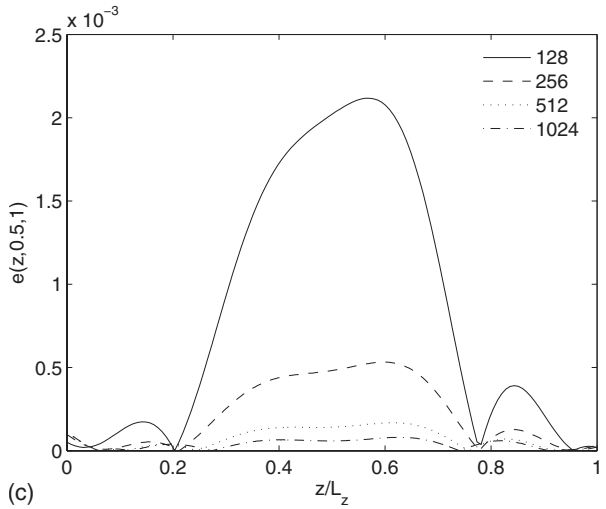


FIG. 1. Difference between the real part of the analytical solution and the model result for $y/L_y=y_0/L_y=0.5$ [see Eq. (18)] for different values of $N_z=N_y$ and taking $v_z=0.02$, $v_y=0.02$, $\Delta_{0z}=\Delta_{0y}=40$, and $m=1/8$. Solid line, $N_z=N_y=128$; dashed line, $N_z=N_y=256$; dotted line, $N_z=N_y=512$; dash-dotted line, $N_z=N_y=1024$. $t/L_t=$ (a) 0.2; (b) 0.6; (c) 1, where $L_t=500$ is the maximum simulated time.

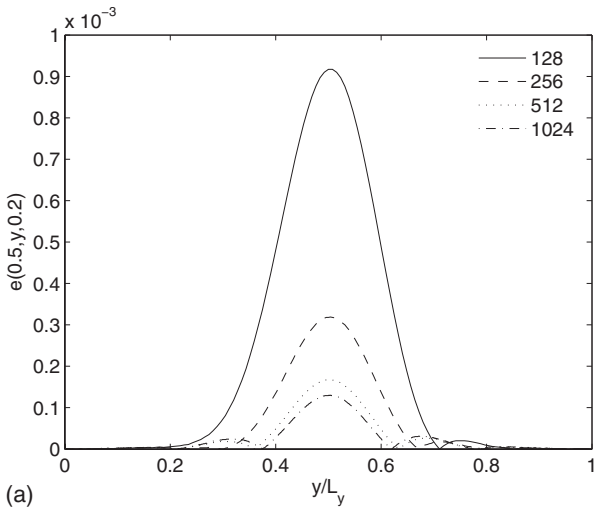


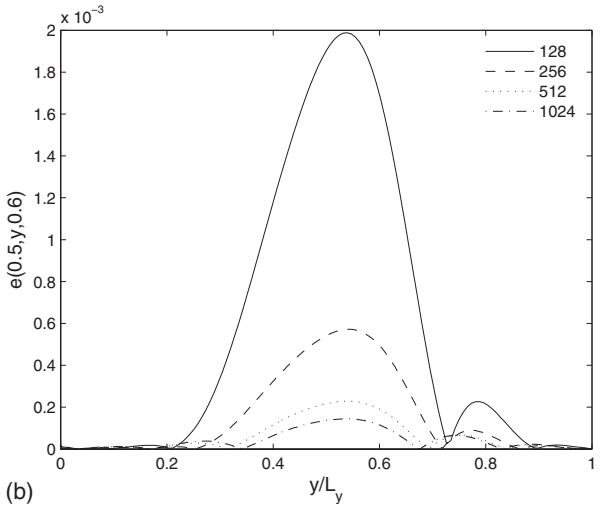


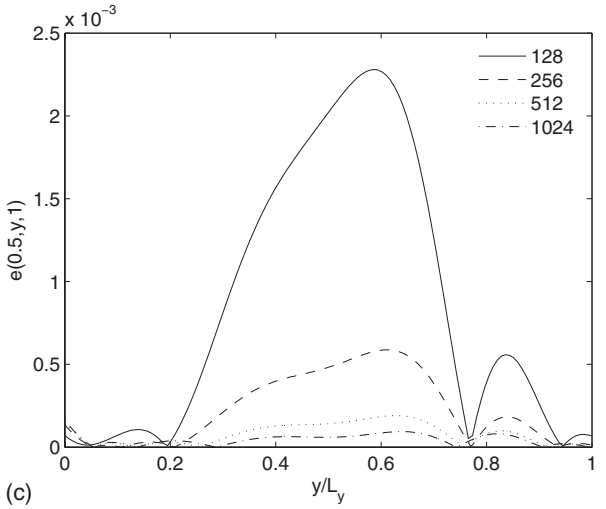


FIG. 2. Difference between the real part of the analytical solution and the model result for $z/L_z=z_0/L_z=0.5$ [see Eq. (18)] for different values of $N_z=N_y$ and taking $v_z=0.02$, $v_y=0.02$, $\Delta_{0z}=\Delta_{0y}=40$, and $m=1/8$. Solid line, $N_z=N_y=128$; dashed line, $N_z=N_y=256$; dotted line, $N_z=N_y=512$; dash-dotted line, $N_z=N_y=1024$. $t/L_t=$ (a) 0.2; (b) 0.6; (c) 1, where $L_t=500$ is the maximum simulated time.

spreads $\Delta_{0z}$ and $\Delta_{0y}$ along $z$ and $y$, respectively, and propagating at speed $(v_z, v_y)$. To impose this initial condition on the model, we set

$$u_1 = u_2 = \frac{1}{2}\psi_0,$$

$$d_1 = d_2 = -i\frac{1}{2}\psi_0.$$

Furthermore, periodic boundary conditions are imposed in all the simulations.

With the initial condition given by Eq. (13), the analytical solution of the Schrödinger equation for a freely propagating particle is given by

$$\psi_{an}(z,y,t) = \left[2\pi\left(\Delta_{0z} + \frac{it}{2m\Delta_{0z}}\right)\left(\Delta_{0y} + \frac{it}{2m\Delta_{0y}}\right)\right]^{-1/2} \times \exp\left(-\frac{(z - z_0 - v_z t)^2}{4\Delta_{0z}^2 + 2it/m}\right) \times \exp\left(-\frac{(y - y_0 - v_y t)^2}{4\Delta_{0y}^2 + 2it/m}\right)\exp[im(v_z z + v_y y)] \times \exp\left(-\frac{im(v_z^2 + v_y^2)t}{2}\right). \quad (14)$$

Based on this solution, the mean position $(Z(t), Y(t))$ and the mean spreads $\Delta_z(t)$ and $\Delta_y(t)$ evolve according to the equations

$$Z(t) = z_0 + v_z t, \quad Y(t) = y_0 + v_y t, \quad (15)$$

and

$$\Delta_z(t) = \left(\Delta_{0z}^2 + \frac{t^2}{4m^2\Delta_{0z}^2}\right)^{1/2},$$

$$\Delta_y(t) = \left(\Delta_{0y}^2 + \frac{t^2}{4m^2\Delta_{0y}^2}\right)^{1/2}. \quad (16)$$

For a free particle, the mean energy $\langle E \rangle$ is given by

$$\langle E \rangle = i\hbar \int \psi^* \partial_t \psi \, dz \, dy = -\frac{\hbar^2}{2m}\int \psi^* \Delta \psi \, dz \, dy$$

$$= \frac{\hbar^2}{2m}\int \nabla\psi^* \nabla \psi \, dz \, dy = \frac{\hbar^2}{2m}\|\nabla\psi\|_2^2.$$

Hence, for the minimum uncertainty wave packet, we obtain

$$\langle E \rangle = \frac{1}{2m}\left(m^2(v_z^2 + v_y^2) + \frac{1}{4\Delta_{0z}^2} + \frac{1}{4\Delta_{0y}^2}\right). \quad (17)$$

Since our model provides four wave functions $\phi_{1,2}^{\pm}$, we can compute $E_{1,2}^{+}$ and $E_{1,2}^{-}$ on $\phi_{1,2}^{+}$ and $\phi_{1,2}^{-}$, respectively, and then define

$$E^+ = E_1^+ + E_2^+, \quad E^- = E_1^- + E_2^-, \quad E = E^+ + E^-.$$

TABLE I. Propagation velocity and spread of the packet at time $t=500$ for different values of $N_z=N_y$. The expected values are $v_z=0.02$, $v_y=0.04$, and $\Delta_z(500)=\Delta_y(500)=64.03$. Here $m=1/8$ and $\Delta_{0z}=\Delta_{0y}=40$.

| $N_z=N_y$ | $v_z$ | $v_y$ | $\Delta_z(500)$ | $\Delta_y(500)$ |
|---|---|---|---|---|
| 128 | 0.0175 | 0.0355 | 60.20 | 60.19 |
| 256 | 0.0189 | 0.0379 | 62.41 | 62.40 |
| 512 | 0.0191 | 0.0384 | 62.97 | 62.95 |
| 1024 | 0.0193 | 0.0386 | 63.11 | 63.09 |

### A. Comparison with the analytical solution and convergence test

To study the convergence of the model, we need to fix the domain $[z_{min}, z_{max}]\times[y_{min}, y_{max}]$ and to discretize it by using an increasing number of points $n_z \times n_y$. Moreover, the lattice must be uniform (i.e., $\Delta z = \Delta y \equiv h$) and the relation $h=\Delta t$ must be preserved (recall that $c=1$ in lattice units). In general, $h$ is given by

$$h = \frac{z_{max} - z_{min}}{n_z - 1} = \frac{y_{max} - y_{min}}{n_y - 1}.$$

This setting implies a change in the scheme which, for the one-dimensional case, consists in multiplying by a factor $h$ the right-hand side of Eq. (2), corresponding to an "effective" mass $m' = hm$. For this reason, we need to take a sufficiently large domain so that $m'$ is not too close to zero.

In this numerical test we set $[z_{min}, z_{max}]\times[y_{min}, y_{max}] = [0,512]\times[0,512]$ and $N_z = n_z - 1$ and $N_y = n_y - 1$ take the values 128, 256, 512, and 1024. The remaining parameters are set as follows: $\Delta_{0z}=\Delta_{0y}=40$, $v_z=0.02$, $v_y=0.04$, and $m=1/8$. The error with respect to the analytical solution Eq. (14) is computed in $L^2$ norm. In particular, we define

$$e_2(t) = \|\psi_{an}(z,y,t) - \phi^+(z,y,t)\|_2 = \left(\int |\psi_{an}(z,y,t) - \phi^+(z,y,t)|^2 dz\, dy\right)^{1/2}.$$

The error $e_2$ was found to decrease from 0.08 to 0.009 as the grid resolution was increased from 128 to 1024 points in each direction, but with no clear evidence of a specific convergence rate. We tentatively interpret this as the concurrent effect of time-discretization errors, $[O(h^2)]$, the splitting error $[O(h)]$ and lack of adiabaticity in the limit $mh \to 0$. In Fig. 1 the function

$$e(z,y,t) = |\mathrm{Re}[\psi_{an}(z,y,t)] - \mathrm{Re}[\phi^+(z,y,t)]| \quad (18)$$

taken at $y=y_0$ for the different values of $N_z$ and $N_y$ is plotted at times 100, 300, and 500. In Fig. 2 the same function evaluated at $z=z_0$ is shown. In Figs. 1 and 2 space is normalized to unit value by plotting, on the abscissa axis, $z/L_z$ and $y/L_y$, respectively. Here, $L_z$ and $L_y$ indicate the domain lengths along $z$ and $y$. For these simulations we have $L_z = L_y = 512$.

In Table I we report the propagation velocity and the

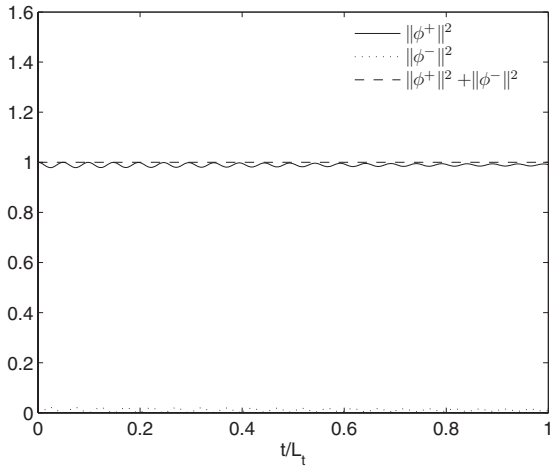


FIG. 3. $\|\phi^+\|^2$ (solid line), $\|\phi^-\|^2$ (dotted line), and $\|\phi^+\|^2+\|\phi^-\|^2$ (dashed line) for $N_z=N_y=1024$ ($h=1/2$), $m=1/8$, $\Delta_{0z}=\Delta_{0y}=40$, $v_z=0.02$, and $v_y=0.04$. Time is normalized by plotting $t/L_t$, where $L_t=500$ is the maximum simulated time.

mean spread of the packet with increasing number of discretization points. For the present setting the expected velocity is $v_z=0.02$ and $v_y=0.04$ and the spread at time $t=500$ is computed by Eq. (16) and is 64.03 since $\Delta_{0z}=\Delta_{0y}=40$.

In the following section we will check the ability of the model to reproduce the mean position and spread for different sets of parameters.

The model is able to preserve a unit norm, i.e., the quantity

$$\|\phi^+\|^2+\|\phi^-\|^2=\int |\phi^+(z,t,t)|^2dz\,dy+\int |\phi^-(z,y,t)|^2dz\,dy.$$

It follows that $\|\phi^+\|=1$ cannot be preserved during the evolution. Indeed, we have $\|\phi^-\|\ll\|\phi^+\|$, with both terms oscillating in such a way that $\|\phi^+\|^2+\|\phi^-\|^2=1$. In Fig. 3 $\|\phi^+\|^2$, $\|\phi^-\|^2$ and $\|\phi^+\|^2+\|\phi^-\|^2$ are shown, while in Fig. 4 only $\|\phi^+\|^2$ is plotted, in order to have a closer appreciation of its evolution.

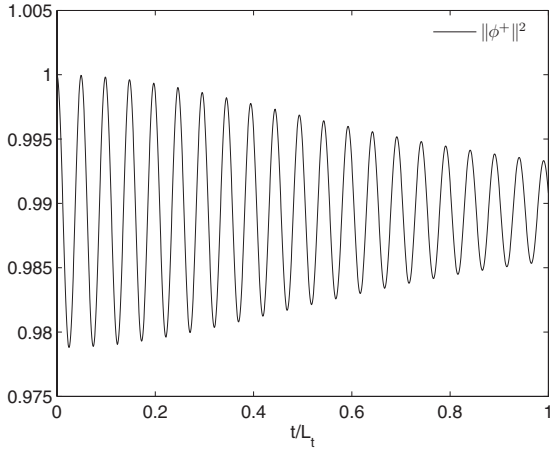


FIG. 4. $\|\phi^+\|^2$ for $N_z=N_y=1024$ ($h=1/2$), $m=1/8$, $\Delta_{0z}=\Delta_{0y}=40$, $v_z=0.02$, and $v_y=0.04$. Time is normalized by plotting $t/L_t$, where $L_t=500$ is the maximum simulated time.

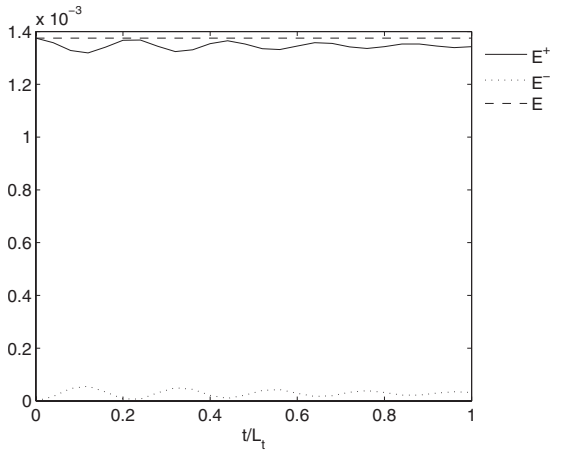


FIG. 5. $E^+$ (solid line), $E^-$ (dotted line), and $E=E^++E^-$ (dashed line) for $N_z=N_y=512$ ($h=1$), $m=1/8$, $\Delta_{0z}=\Delta_{0y}=40$, $v_z=0.02$, and $v_y=0.04$. Time is normalized by plotting $t/L_t$, where $L_t=500$ is the maximum simulated time. The energy is expressed in lattice units.

A similar behavior is obtained for the energy. The model stays constant, and very close to the expected value given by Eq. (17), the total kinetic energy $E=E^++E^-$, while $E^+$ and $E^-$ are oscillating with $E^-\ll E^+$. In Fig. 5 $E^+$, $E^-$ and $E$ are shown.

Finally, in Table II we report the mean values of $\|\phi^+\|^2$, $E^+$, and $E$ while increasing the number of nodes. Note that, for the present setting, the expected value for the energy given by Eq. (17) is $1.375\times10^{-3}$.

### B. Mean position and mean spreads

In all of the following simulations we take $h\equiv\Delta z=\Delta t=1$; hence the computational domain is $[0,n_z]\times[0,n_y]$ and is not fixed as in the previous section. In all of the simulations periodic boundary conditions are imposed.

As we mentioned, the mean position and mean spreads evolve according to Eqs. (15) and (16). We can check the ability of the model to reproduce these evolutions under a number of different conditions.

In all of the following tests we use a grid of size $1024\times1024$. As to the position, we measure the propagation velocity of the packet for different values of the parameters $m$ and $\Delta_{0z}=\Delta_{0y}$, while keeping $v_z=0.05$ and $v_y=0.025$. In Table III, the results of the model are reported.

To verify the asymptotic behavior of $\Delta_z(t)$ and $\Delta_t(t)$ we set $v_z=v_y=0$ so that the wave packet is not hitting the grid

TABLE II. Mean values of $\|\phi^+\|^2$, $E^+$, and $E$ for different values of $N_z=N_y$. The expected value for the energy is $1.375\times10^{-3}$. Here $m=1/8$, $\Delta_{0z}=\Delta_{0y}=40$, $v_z=0.02$, and $v_y=0.04$.

| $N_z=N_y$ | $\|\phi^+\|^2$ | $E^+$ | $E$ |
|---|---|---|---|
| 128 | 0.980 | $1.234\times10^{-3}$ | $1.3712\times10^{-3}$ |
| 256 | 0.985 | $1.240\times10^{-3}$ | $1.3741\times10^{-3}$ |
| 512 | 0.987 | $1.293\times10^{-3}$ | $1.3748\times10^{-3}$ |
| 1024 | 0.988 | $1.320\times10^{-3}$ | $1.3749\times10^{-3}$ |

TABLE III. Results for the propagation velocity for different values of $m$ and $\Delta_{0z}=\Delta_{0y}\equiv\Delta_0$. By $R_z$ and $R_y$ are indicated the ratios between the model result and the expected value along $z$ and $y$ respectively. Here $n_z=n_y=1024$, $v_z=0.05$, and $v_y=0.025$.

| $\Delta_0$ | $m$ | $v_z$ | $v_y$ | $R_z$ | $R_y$ |
|---|---|---|---|---|---|
| 50 | 0.1 | 0.048 | 0.024 | 1.038 | 1.040 |
| 32 | 0.1 | 0.047 | 0.023 | 1.073 | 1.076 |
| 32 | 0.2 | 0.048 | 0.024 | 1.034 | 1.035 |
| 16 | 0.2 | 0.046 | 0.023 | 1.084 | 1.092 |

TABLE IV. Asymptotic behavior of $\Delta_z(t)$ and $\Delta_y(t)$ for different values of $m$ and $\Delta_{0z}=\Delta_{0y}\equiv\Delta_0$. By $R_z$ and $R_y$ are indicated the ratios between the model result and the expected value along $z$ and $y$ respectively. Here $n_z=n_y=1024$ and $v_z=v_y=0$.

| $\Delta_0$ | $m$ | $\Delta_z$ | $\Delta_y$ | Expected value | $R_z$ | $R_y$ |
|---|---|---|---|---|---|---|
| 50 | 0.1 | 0.087 | 0.087 | 0.1 | 1.155 | 1.115 |
| 32 | 0.1 | 0.144 | 0.144 | 0.15625 | 1.083 | 1.083 |
| 32 | 0.2 | 0.0719 | 0.0719 | 0.078125 | 1.083 | 1.083 |
| 16 | 0.2 | 0.145 | 0.145 | 0.15625 | 1.080 | 1.080 |

boundary too early. The results are reported in Table IV.

Finally, we set $v_z\neq v_y$ and $\Delta_{0z}\neq\Delta_{0y}$, in particular we choose $v_z=0.05$, $v_y=0.02$, $\Delta_{0z}=50$, $\Delta_{0y}=32$, and $m=0.2$. In Fig. 6, we compare $Z(t)$ and $\Delta_z(t)$ with the analytical curves given by Eqs. (15) and (16). A similar comparison for $Y(t)$ and $\Delta_y(t)$ is shown in Fig. 7.

## V. NUMERICAL TEST 2: HARMONIC OSCILLATOR

As a second example, we consider a two-dimensional harmonic oscillator. The potential is given by

$$V(z,y)=V_0\left[\left(\frac{z-n_z/2}{n_z/2}\right)^2+\left(\frac{y-n_y/2}{n_y/2}\right)^2\right]$$

and the initial condition is still given by the minimum uncertainty wave packet of Eq. (13); periodic boundary conditions are again assumed.

It is known that the mean quantities $(Z(t),Y(t))$ and $P(t)=(P_z(t),P_y(t))$ obey the classical equations of motion of the harmonic oscillator

$$\dot{Z}=P_z(t)/m,\quad \dot{Y}=P_y(t)/m,$$

$$\ddot{Z}+\omega_0^2 Z=0,\quad \ddot{Y}+\omega_0^2 Y=0;$$

hence,

$$Z(t)=z_0+\frac{v_z}{\omega_0}\sin(\omega_0 t),$$

$$Y(t)=y_0+\frac{v_y}{\omega_0}\sin(\omega_0 t). \tag{19}$$

Moreover, if we set $\Delta_{0z}=\Delta_{0y}\equiv\Delta_0$ such that

$$\omega_0=\frac{1}{2m\Delta_0^2}, \tag{20}$$

then the initial spreading $\Delta_0$ is preserved all along the evolution. We can check the ability of the model to preserve $\Delta_0$ varying the parameters $V_0$, $m$ and $n_z=n_y$ so as to produce the following spreadings: $\Delta_0=64$, 32, and 16. In Table V the model results are reported. Here $\Delta_z$ and $\Delta_y$ are the wave function variances averaged over two periods. In all of the simulations we set $v_z=0.02$ and $v_y=0.04$. In Fig. 8, $Z(t)$ and

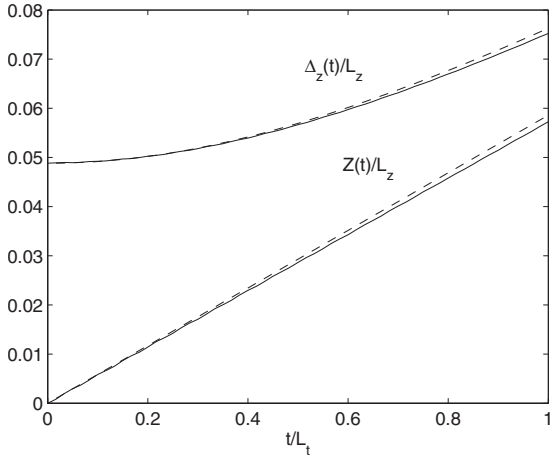


FIG. 6. Comparison between $Z(t)$ and $\Delta_z(t)$ and the expected curves given by Eqs. (15) and (16) for the following settings: $n_z=n_y=1024$, $v_z=0.05$, $v_y=0.02$, $\Delta_{0z}=50$, $\Delta_{0y}=32$, and $m=0.2$. Solid lines represent $Z(t)$ and $\Delta_z(t)$ given by the model; dashed lines are the expected curves. Time is normalized by plotting $t/L_t$, where $L_t=1200$ is the maximum simulated time. Space is also normalized to unit value by plotting $Z(t)/L_z$ and $\Delta_z(t)/L_z$, where $L_z=1024$ is the domain width along the $z$ axis.

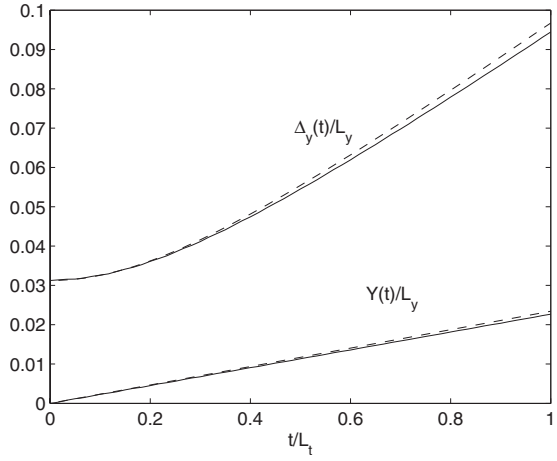


FIG. 7. Comparison between $Y(t)$ and $\Delta_y(t)$ and the expected curves given by Eqs. (15) and (16) for the following settings: $n_z=n_y=1024$, $v_z=0.05$, $v_y=0.02$, $\Delta_{0z}=50$, $\Delta_{0y}=32$, and $m=0.2$. Solid lines represent $Y(t)$ and $\Delta_y(t)$ given by the model; dashed lines are the expected curves. Time is normalized by plotting $t/L_t$, where $L_t=1200$ is the maximum simulated time. Space is also normalized to unit value by plotting $Y(t)/L_y$ and $\Delta_y(t)/L_y$, where $L_y=1024$ is the domain width along the $y$ axis.

TABLE V. Averaged variances of the packet along $z$ and $y$ for different settings of the parameters $n_z=n_y$, $m$ and $V_0$. Here $v_z=0.02$ and $v_y=0.04$.

| $n_z=n_y$ | $V_0$ | $m$ | $\Delta_z$ | $\Delta_y$ | Expected $\Delta$ |
|---|---|---|---|---|---|
| 1024 | 1/32 | 1/16 | 64.35±1.33 | 64.35±1.33 | 64 |
| 1024 | 1/8 | 1/4 | 32.25±0.70 | 32.27±0.75 | 32 |
| 512 | 1/16 | 1/8 | 32.16±0.70 | 32.17±0.69 | 32 |
| 512 | 1/32 | 1/4 | 31.87±0.27 | 31.87±0.29 | 32 |
| 512 | 1/4 | 1/2 | 16.01±0.69 | 16.02±0.70 | 16 |
| 256 | 1/8 | 1/4 | 16.05±0.37 | 16.05±0.38 | 16 |
| 256 | 1/16 | 1/2 | 15.74±0.32 | 15.74±0.32 | 16 |

$\Delta_z(t)$ are shown for $n_z=n_y=512$, $V_0=1/32$, $m=1/4$; in Fig. 9, $Y(t)$ and $\Delta_y(t)$ are reported for the same set of parameters.

When an external potential $V$ is acting on the particle, as in this case, the total energy of a wave function $\psi$ satisfying the Schrödinger equation is given by

$$\langle E\rangle = i\hbar \int \psi^* \partial_t \psi \, dz \, dy$$

$$= \frac{\hbar^2}{2m} \int \nabla\psi^* \nabla \psi \, dz \, dy + \int \psi^* V \psi \, dz \, dy.$$

In analogy with classical mechanics, $\langle E\rangle$ satisfies the relation

$$\langle E\rangle = \frac{1}{2m}\langle P^2\rangle + \langle V\rangle.$$

In Fig. 10 the kinetic and potential energy and their sum are plotted for the harmonic oscillator defined by the parameters $n_z=n_y=512$, $V_0=1/32$, $m=1/4$. In particular, the energies are computed using $\phi^+_{1,2}$; the quantities $E^+_{kin}$, $E^+_{pot}$, and $E^+=E^+_{kin}+E^+_{pot}$ are shown independently. From this figure, a satisfactory energy conservation is observed.

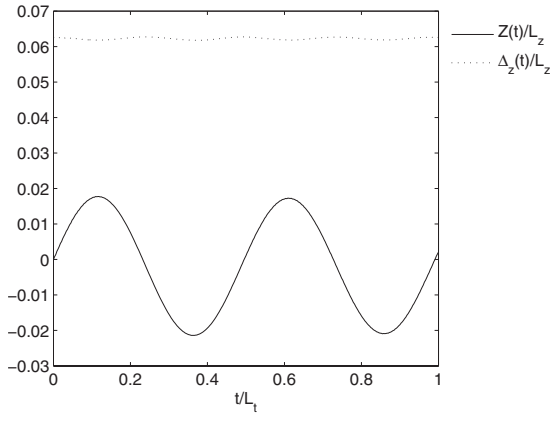


FIG. 8. $Z(t)$ and $\Delta_z(t)$ for the harmonic oscillator with parameters $n_z=n_y=512$, $V_0=1/32$, $m=1/4$, $v_z=0.02$, and $v_y=0.04$. The solid line is $Z(t)$, while the dotted one is $\Delta_z(t)$. Time is normalized by plotting $t/L_t$, where $L_t=6600$ is the maximum simulated time. Space is also normalized to unit value by plotting $Z(t)/L_z$ and $\Delta_z(t)/L_z$, where $L_z=512$ is the domain width along the $z$ axis.

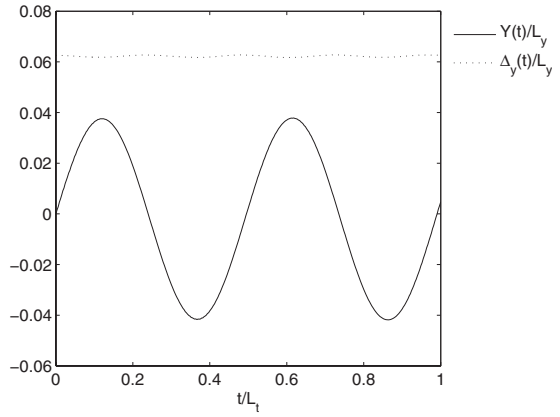


FIG. 9. $Y(t)$ and $\Delta_y(t)$ for the harmonic oscillator with parameters $n_z=n_y=512$, $V_0=1/32$, $m=1/4$, $v_z=0.02$, and $v_y=0.04$. The solid line is $Y(t)$, while the dotted one is $\Delta_y(t)$. Time is normalized by plotting $t/L_t$, where $L_t=6600$ is the maximum simulated time. Space is also normalized to unit value by plotting $Y(t)/L_y$ and $\Delta_y(t)/L_y$, where $L_y=512$ is the domain width along the $y$ axis.

Finally, in order to verify the isotropy of the model we plot the isolines taken at some values of $\rho=|\psi(z,y)|^2$. This test is performed for the following set of parameters: $n_z=n_y=256$, $V_0=1/8$, $m=1/4$. The contour plot obtained after two periods is shown in Fig. 11. In particular, the isolines taken at $\rho=1\times10^{-4}$, $2\times10^{-4}$, $3\times10^{-4}$, $4\times10^{-4}$, $5\times10^{-4}$, and $6\times10^{-4}$ are plotted.

## VI. NUMERICAL TEST 3: ROTATED ELLIPTIC OSCILLATOR

As a third test we model an elliptic oscillator by using the potential

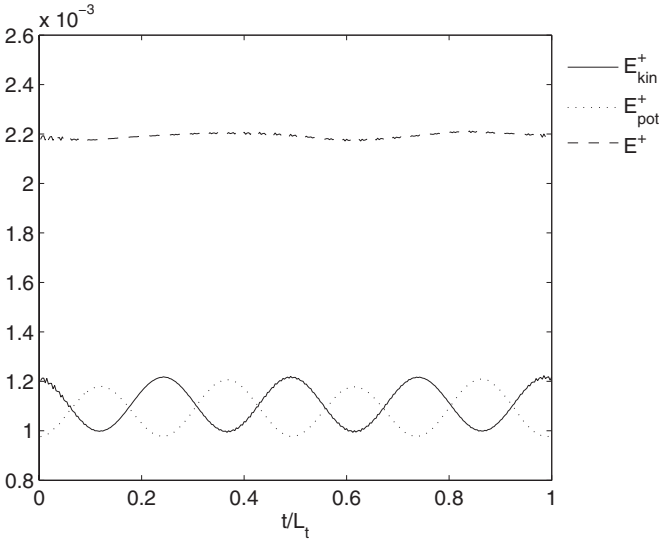


FIG. 10. $E^+_{kin}$, $E^+_{pot}$, and $E^+=E^+_{kin}+E^+_{pot}$ for the harmonic oscillator with parameters $n_z=n_y=512$, $V_0=1/32$, $m=1/4$, $v_z=0.02$, and $v_y=0.04$. Solid line, $E^+_{kin}$; dotted line, $E^+_{pot}$; dashed line, $E^+=E^+_{kin}+E^+_{pot}$. Time is normalized by plotting $t/L_t$, where $L_t=6600$ is the maximum simulated time. The energy is expressed in lattice units.

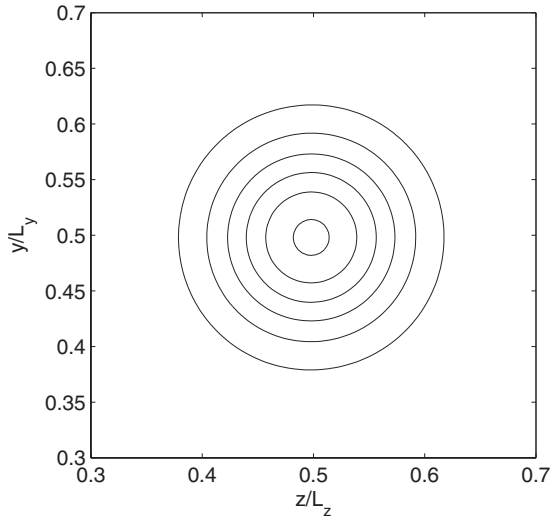


FIG. 11. Contour plot for $\rho=|\psi(z,y)|^2$ for the harmonic oscillator with parameters $n_z=n_y=256$, $V_0=1/8$, $m=1/4$, $v_z=v_y=0.0$, and $\Delta_0=16$. Here, coordinates $z$ and $y$ are normalized to unit value by plotting the dimensionless quantities $z/L_z$ and $y/L_y$, where $L_z=L_y=256$ are the domain lengths along $z$ and $y$, respectively. The isolines correspond to the following values of $\rho$: $1\times10^{-4}$, $2\times10^{-4}$, $3\times10^{-4}$, $4\times10^{-4}$, $5\times10^{-4}$, and $6\times10^{-4}$ going from the outside toward the inside.

$$V(z,y)=V_0\left[\frac{1}{a^2}\left(\frac{z-n_z/2}{n_z/2}\right)^2+\frac{1}{b^2}\left(\frac{y-n_y/2}{n_y/2}\right)^2\right],$$

where we take $n_z=n_y\equiv n$.

If we define

$$\omega_0=\sqrt{\frac{2V_0}{m}}\frac{1}{n/2},$$

then the characteristic frequencies along $z$ and $y$ are given by

$$\omega_{0z}^2=\frac{\omega_0^2}{a^2},\quad \omega_{0y}^2=\frac{\omega_0^2}{b^2}.$$

The evolution of $Z(t)$ and $Y(t)$ is described by

$$Z(t)=\frac{v_z}{\omega_{0z}}\sin(\omega_{0z}t),$$

$$Y(t)=\frac{v_y}{\omega_{0y}}\sin(\omega_{0y}t),$$

and choosing $\Delta_{0z}$ and $\Delta_{0y}$ such that

$$\omega_{0z}=\frac{1}{2m\Delta_{0z}^2},\quad \omega_{0y}=\frac{1}{2m\Delta_{0y}^2},\tag{21}$$

the initial spreadings are preserved throughout the evolution.

Consider, now, a rotated coordinate system

$$z'=z\cos(\alpha)-y\sin(\alpha),$$

$$y'=z\sin(\alpha)+y\cos(\alpha).\tag{22}$$

The mean position in the rotated system $(Z'(t),Y'(t))$, is still following the laws

$$Z'(t)=\frac{v_{z'}}{\omega_{0z}}\sin(\omega_{0z}t),$$

$$Y'(t)=\frac{v_{y'}}{\omega_{0y}}\sin(\omega_{0y}t),\tag{23}$$

and, from Eq. (22), we have that $(Z(t),Y(t))$ must satisfy

$$Z(t)=Z'(t)\cos(\alpha)+Y'(t)\sin(\alpha),$$

$$Y(t)=-Z'(t)\sin(\alpha)+Y'(t)\cos(\alpha).\tag{24}$$

We next check the ability of the model to reproduce these evolutions for $Z(t)$ and $Y(t)$ for this elliptic rotated oscillator.

As a first example, we set the parameters as follows: $n=1024$, $a^2=2$, $b^2=4$, $m=1/8$, $V_0=1/16$, $v_{z'}=0.05$, $v_{y'}=0$, and $\alpha=\pi/4$. With this setting we have

$$\omega_0=\frac{1}{512},\quad \omega_{0z}=\frac{1}{\sqrt{2}512},\quad \omega_{0y}=\frac{1}{1024},$$

and, from Eq. (21), we obtain

$$\Delta_{0z}=53.817,\quad \Delta_{0y}=64.$$

Moreover, since $v_{y'=0}$, from Eqs. (23) and (24), we expect the following evolution for $Z(t)$ and $Y(t)$:

$$Z(t)=\frac{v_{z'}}{\omega_{0z}}\sin(\omega_{0z}t)\cos(\alpha)=\frac{v_{z'}}{\omega_{0z}}\sin(\omega_{0z}t)\frac{\sqrt{2}}{2},$$

$$Y(t)=-\frac{v_{z'}}{\omega_{0z}}\sin(\omega_{0z}t)\sin(\alpha)=-\frac{v_{z'}}{\omega_{0z}}\sin(\omega_{0z}t)\frac{\sqrt{2}}{2}.$$

In Fig. 12, $Z(t)$ and $Y(t)$ are plotted. We also observe that

$$\frac{v_{z'}}{\omega_{0z}}\frac{\sqrt{2}}{2}=25.6,$$

in close agreement with the maximum absolute value reached by $Z(t)$ and $Y(t)$, which is 25.47, corresponding to $Z(t)/L_z=Y(t)/L_y=0.0248$ as indicated in Fig. 12 (where $L_z=L_y=1024$ are the domain widths along $z$ and $y$).

As a second example we set $n=1024$, $a^2=1$, $b^2=2$, $m=1/4$, $V_0=1/32$, $v_{z'}=0.05$, $v_{y'}=0.0$, and $\alpha=\pi/6$. With these parameters we obtain

$$\omega_0=\frac{1}{1024},\quad \omega_{0z}=\frac{1}{1024},\quad \omega_{0y}=\frac{1}{\sqrt{2}1024},$$

and, from Eq. (21),

$$\Delta_{0z}=45.255,\quad \Delta_{0y}=53.817.$$

As in the previous example, since $v_{y'=0}$, from Eqs. (23) and (24), we expect the following evolution for $Z(t)$ and $Y(t)$:

$$Z(t)=\frac{v_{z'}}{\omega_{0z}}\sin(\omega_{0z}t)\cos(\alpha)=\frac{v_{z'}}{\omega_{0z}}\sin(\omega_{0z}t)\frac{\sqrt{3}}{2},$$

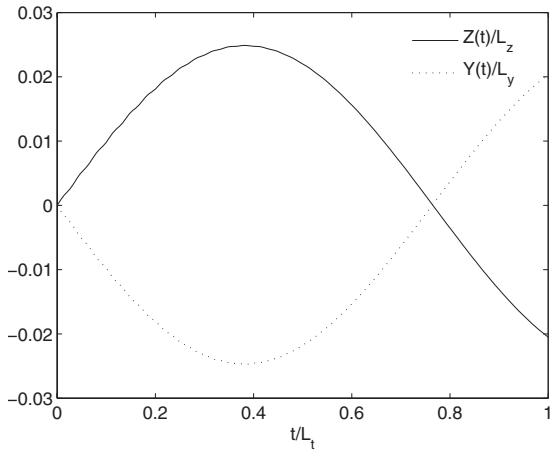


FIG. 12. $Z(t)$ and $Y(t)$ for the rotated elliptic oscillator of the first test. The solid line is $Z(t)$, while the dotted one is $Y(t)$. In this first test, the parameters are as follows: $n=1024$, $a^2=2$, $b^2=4$, $m=1/8$, $V_0=1/16$, $v_{z'}=0.05$, $v_{y'}=0$, and $\alpha=\pi/4$. Time is normalized by plotting $t/L_t$, where $L_t=3000$ is the maximum simulated time. Space is also normalized to unit value by plotting $Z(t)/L_z$ and $Y(t)/L_y$, where $L_z=L_y=1024$ are the domain widths along $z$ and $y$.

$$Y(t) = -\frac{v_{z'}}{\omega_{0z}}\sin(\omega_{0z}t)\sin(\alpha) = -\frac{v_{z'}}{\omega_{0z}}\sin(\omega_{0z}t)\frac{1}{2}.$$

In Fig. 13, $Z(t)$ and $Y(t)$ are plotted. We also observe that

$$\frac{v_{z'}}{\omega_{0z}}\frac{\sqrt{3}}{2} = 44.34, \quad \frac{v_{z'}}{\omega_{0z}}\frac{1}{2} = 25.6,$$

again in close agreement with the maximum absolute values reached by $Z(t)$ and $Y(t)$, namely, 43.90 and 25.27, corresponding to $Z(t)/L_z=0.0429$ and $Y(t)/L_y=0.0247$ as indicated in Fig. 13 (where $L_z=L_y=1024$ are the domain widths along $z$ and $y$).

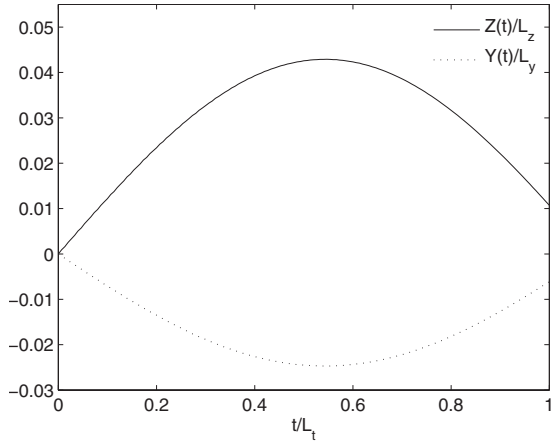


FIG. 13. $Z(t)$ and $Y(t)$ for the rotated elliptic oscillator of the second test. The solid line is $Z(t)$, while the dotted one is $Y(t)$. In this second test, the parameters are as follows: $n=1024$, $a^2=1$, $b^2=2$, $m=1/4$, $V_0=1/32$, $v_{z'}=0.05$, $v_{y'}=0.0$, and $\alpha=\pi/6$. Time is normalized by plotting $t/L_t$, where $L_t=3000$ is the maximum simulated time. Space is also normalized to unit value by plotting $Z(t)/L_z$ and $Y(t)/L_y$, where $L_z=L_y=1024$ are the domain widths along $z$ and $y$.

## VII. THREE-DIMENSIONAL MODEL

The two-dimensional model just described can be easily extended to three dimensions. In this case, as a result of the application of transformation $Z$ [see Eq. (6)], the Dirac equation takes the form

$$[\partial_t + A_x\partial_z + A_y\partial_y + A_z\partial_z]\psi = C\psi,$$

$$\psi(x,y,z,0) = \psi_0(x,y,z),$$

where $A_y$, $A_z$, and $C$ are the same as in Eq. (7) and

$$A_x = \begin{pmatrix} 0 & 0 & 0 & 1 \\ 0 & 0 & -1 & 0 \\ 0 & -1 & 0 & 0 \\ 1 & 0 & 0 & 0 \end{pmatrix}.$$

By using the sequential splitting method, we consider the sequence of three initial value problems for $(n-1)\Delta t < t \leq n\Delta t$

$$\partial_t\psi_1^n + A_x\partial_x\psi_1^n = \frac{1}{3}C\psi_1^n,$$

$$\psi_1^n[(n-1)\Delta t] = \psi_3^{n-1}((n-1)\Delta t), \tag{25}$$

$$\partial_t\psi_2^n + A_y\partial_y\psi_2^n = \frac{1}{3}C\psi_2^n$$

$$\psi_2^n[(n-1)\Delta t] = \psi_1^n(n\Delta t),$$

and

$$\partial_t\psi_3^n + A_z\partial_z\psi_3^n = \frac{1}{3}C\psi_3^n$$

$$\psi_3^n[(n-1)\Delta t] = \psi_2^n(n\Delta t).$$

To start the procedure, we set $\psi_3^0(0)=\psi_0$ and $\psi_{sp}(x,y,z,n\Delta t)=\psi_3^n(x,y,z,n\Delta t)$ is the splitting solution of the problem.

To solve the problem of Eq. (25) with a one-dimensional lattice Boltzmann model, $A_x$ needs to be diagonalized. A possible choice for the transformation matrix is given by

$$X = \frac{1}{\sqrt{2}}\begin{pmatrix} -1 & 0 & 1 & 0 \\ 0 & 1 & 0 & -1 \\ 1 & 0 & 1 & 0 \\ 0 & 1 & 0 & 1 \end{pmatrix}.$$

The three-dimensional algorithm set proceeds in full analogy with the two-dimensional case.

### Numerical test: Harmonic oscillator

In order to test the isotropy of the three-dimensional model, we simulate a three-dimensional harmonic oscillator

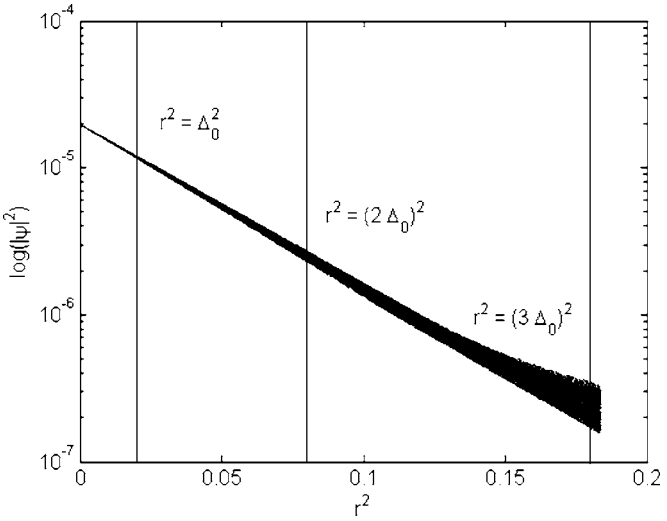


FIG. 14. Scatter plot of $|\psi(x,y,z)|^2$ against $r^2$ for a three-dimensional harmonic oscillator with parameters $n_z=n_y=n_z=100$, $V_0=0.081\,35$, $m=0.1$, $v_x=v_y=v_z=0$, and $\Delta_0=14$ at time $t=T/4$. $|\psi(x,y,z)|^2$ is represented on a logarithmic scale in order to show its linear dependence on $r^2$. Here, the coordinates $x$, $y$, and $z$ are normalized to unit value by plotting the dimensionless quantities $x/L_x$, $y/L_y$, and $z/L_z$, where $L_x=L_y=L_z=100$ are the domain lengths along $x$, $y$, and $z$, respectively.

and we show that by fixing $\Delta_{0x}=\Delta_{0y}=\Delta_{0z}\equiv\Delta_0$ such that

$$\omega_0=\frac{1}{2m\Delta_0^2}, \tag{26}$$

the packet spreading is kept constant throughout the evolution.

For this test we set $nx=ny=nz=100$, $V_0=0.081\,35$, $m=0.1$, $v_x=v_y=v_z=0$, and periodic boundary conditions are imposed. With this setting we have $\omega_0=0.025\,51$ and, from Eq. (26), we obtain $\Delta_0=14$. The numerical values given by the model for $\Delta_x$, $\Delta_y$, and $\Delta_z$ averaged over a quarter of a period are

$$\Delta_x=15.35\pm1.38,\quad \Delta_y=14.40\pm0.88,\quad \Delta_z=15.47\pm1.50.$$

Let us consider the radius $r$ defined as $r^2=(x-x_0)^2+(y-y_0)^2+(z-z_0)^2$, where the point $(x_0,y_0,z_0)$ is the center of the initial Gaussian wave packet. In Fig. 14, a scatter plot of $|\psi(x,y,z)|^2$ against $r^2$ at time $t=T/4$ (where $T$ is the harmonic oscillator period, $T=2\pi/\omega_0\approx250$ lattice units) is reported in order to expose the degree of isotropy of the numerical solution. In the figure, results are shown for $r^2<(3\Delta_0)^2$, because for larger values of $r^2$, statistical fluctuations become dominant due to the extremely small values of $|\psi|^2$. To be noted that, due again to the exponential dependence of $|\psi|^2$ on the radius ($|\psi|^2\sim e^{-r^2/(2\Delta_0^2)}$), even a mild lack of isotropy is exponentially enhanced at increasing values of $r$. This effect is well visible in Fig. 14. However, for $r^2<\Delta_0^2$, the linear dependence of $\log(|\psi|^2)$ on $r^2$ is clearly visible, with a fairly acceptable scatter of the numerical data. For increasing values of $r^2$, however, the scatter also increases. Finally, for $r^2$ close to $(3\Delta_0)^2$, boundary condition effects start to become appreciable. In fact, we note that the solution is not affected by periodic boundary conditions as long as the wave function remains negligible at the boundary. Going much further in time with this setting is not sensible, since the finite-size effects due to the periodic boundary conditions would propagate into the domain, thus deteriorating the solution even for smaller values of $r^2$. To overcome this limitation, a much larger domain, or different boundary conditions, should be used.

## VIII. CONCLUSIONS AND OUTLOOK

The present work explicitly demonstrates the viability of the quantum lattice Boltzmann scheme for the numerical solution of the time-dependent Schrödinger equation in *multiple* spatial dimensions. In addition, it clarifies its links with sequential splitting methods for partial differential equations. Being based on a unitary, first-order, relativistic formulation, at variance with most explicit schemes for nonrelativistic quantum wave equations, the QLB method offers unconditional stability with the size of the time step or mesh. However, its accuracy is subject to the condition $\omega_c\Delta t=\Delta x/\lambda_B\leq1$, $\lambda_B=c/\omega_C$ being the de Broglie wavelength of the particle. Since the time step scales linearly with the mesh spacing (a result of the relativistic formulation), the QLB method can be taken down to very refined grids without suffering the time-step collapse typical of nonrelativistic Courant-Friedrichs-Lewy stability conditions, $\Delta t<(2m/\hbar)\Delta x^2$, thus compensating for its low-order accuracy. However, care must be taken to ensure that errors due to lack of adiabaticity remain under control when $\omega_c\Delta t$ is sent to zero. Due to the one-sided nature of the space-time discretization, the light-cone streaming, as well as its low communication to computation ratio, the QLB method makes an excellent candidate for parallel implementations on classical (electronic) computers, as well as for prospective quantum computing applications [18–20]. Indeed, the complex distribution function $\psi(x,t)=c_u u(x,t)+c_d d(x,t)$, $c_u$ and $c_d$ being two complex coefficients, provides a natural representation of qubits as an arbitrary superposition of the two quantum eigenstates $u(x,t)$ and $d(x,t)$ at each space-time location $(x,t)$. Moreover, as observed in [21], the stream-and-collide structure of the quantum lattice Boltzmann equation maps naturally onto the structure of quantum networks, i.e., quantum computing devices consisting of quantum logic gates, whose computational operation proceeds synchronously in time. The output of some gates is wire connected to the input of some others (the streaming step), and locally processed by unitary operations (the collision step).

In addition to the quantum computing prospects, further extensions to nonlinear quantum wave equations, e.g., the Gross-Pitaevski equation describing zero-temperature Bose-Einstein condensates [22], as well as to nonuniform grids, make interesting topics of future research in the field.

## ACKNOWLEDGMENTS

Professor R. Spigler and J. Acebron are kindly acknowledged for many valuable discussions.

[1] G. McNamara and G. Zanetti, Phys. Rev. Lett. **61**, 2332 (1988).
[2] F. Higuera and J. Jimenez, Europhys. Lett. **9**, 663 (1989).
[3] R. Benzi, S. Succi, and M. Vergassola, Phys. Rep. **222**, 145 (1992).
[4] S. Succi and P. Vergari, VLSI Des. **6**, 137 (1998).
[5] B. M. Boghosian and W. Taylor, Physica D **120**, 30 (1998).
[6] B. M. Boghosian and Washington Taylor IV, Phys. Rev. E **57**, 54 (1998).
[7] I. Bialynicki-Birula, Phys. Rev. D **49**, 6920 (1994).
[8] D. A. Meyer, J. Stat. Phys. **85**, 551 (1996).
[9] D. A. Meyer, Int. J. Mod. Phys. C **8**, 717 (1997).
[10] S. Succi and R. Benzi, Physica D **69**, 327 (1993).
[11] S. Succi, Phys. Rev. E **53**, 1969 (1996).
[12] S. Succi, in *Kinetic Approach to Lattice Quantum Mechanics*, Lecture Notes in Computer Science Vol. 2493 (Springer-Verlag, Berlin, 2002), p. 114.
[13] L. Landau and E. Lifshitz, *Relativistic Quantum Field Theory* (Pergamon, Oxford, 1960).
[14] X. He, S. Chen, and G. D. Doolen, J. Comput. Phys. **146**, 282 (1998).
[15] F. Higuera, S. Succi, and R. Benzi, Europhys. Lett. **9**, 345 (1989).
[16] *Time Dependent Methods for Quantum Mechanics*, edited by K. C. Kulander, (North-Holland, Amsterdam, 1991).
[17] Simultaneous diagonalization of the three matrices $\boldsymbol{L}=(\alpha^x,\beta,-\alpha^z)$ is impossible because particles with spin $s=1/2$ can take only two orientations in space, say $\pm z$; hence they cannot be aligned with more than one dimension at a time.
[18] J. Yepez, Comput. Phys. Commun. **146**, 277 (2002).
[19] J. Yepez, Phys. Rev. E **63**, 046702 (2001).
[20] G. Vahala, J. Yepez, and L. Vahala, Phys. Lett. A **310**, 187 (2003).
[21] P. Love and B. Boghosian, Physica A **362**, 210 (2006).
[22] A. Minguzzi, S. Succi, F. Toschi, M. P. Tosi, and P. Vignolo, Phys. Rep. **395**, 223 (2004).